Shannon Capacity of LOS MIMO Channels with Uniform Circular Arrays

Shannon Capacity of LOS MIMO Channels with Uniform Circular Arrays

Liqin Ding*, Artem R. Vilenskiy†, Rahul Devassy‡, Mikael Coldrey‡, Thomas Eriksson*, Erik G. Ström,*
* Communication Systems Group, Dept. of Electrical Engineering, Chalmers University of Technology, Gothenburg, Sweden
† Antenna Systems Group, Dept. of Electrical Engineering, Chalmers University of Technology, Gothenburg, Sweden
‡ Ericsson Research, Ericsson AB, Gothenburg, Sweden
Email: {liqind, artem.vilenskiy}@chalmers.se, {rahul.devassy, mikael.coldrey}@ericsson.com

***Abstract*—The Shannon capacity for the line-of-sight (LOS) multiple-input multiple-output (MIMO) channel between two perfectly aligned uniform circular arrays (UCAs) is derived from the first principles in a tutorial fashion. It is well known that harmonically related complex exponentials (also known in the literature as orbital angular momentum (OAM) modes) are eigenmodes for the spatially continuous channel. We show that the corresponding eigenvalues can be expressed as Bessel functions of the first kind. We also show that the spatially discrete channel between two UCAs with the same finite number of Hertzian dipole antennas on both sides has eigenmodes that are spatially sampled continuous OAM modes, and discrete eigenvalues that are aliased versions of the continuous eigenvalues. Through numerical solution of Maxwell's equations, we verify that the discrete eigenvalues for UCAs with realistic dipole antennas are the same as with the Hertzian dipoles for the studied geometries (1 km hop distance, UCA radius 1 and 2 m, carrier frequency 70 GHz) as long as antenna spacing is not very dense.**

***Index Terms*—Degrees of freedom, LOS MIMO, UCA, OAM, Eigenmodes.**

I. Introduction

Line-of-sight (LOS) multiple-input multiple-output (MIMO) communication is a key enabler for beyond 100 Gbps and towards 1 Tbps wireless communications. In particular, it is instrumental for spectral efficient wireless transport communication that supports carrier-grade requirements on data rates, availability, and latency in 5G and beyond networks. The key to the analysis and design of LOS MIMO systems is, of course, a good understanding of how the transmitting and receiving antenna geometries, transmission length, and carrier frequency affect the Shannon channel capacity.

The aim of this paper is to shed some new light on this old problem. In particular, we aim to provide rigorous and easy-to-use expressions for the channel capacity for LOS MIMO with uniform circular arrays (UCAs) [1], [2]. To this aim, we start by analyzing the case where two perfectly aligned continuous circular antennas (CAs) are used for transmitting and receiving. From the first principles (Maxwell's equations), we derive analytical expressions for the eigenmodes and the corresponding eigenvalues for the resulting spatial channel. The channel eigenmodes are shown to be the orbital angular momentum (OAM) modes [3], [4], and the eigenvalues are expressions of the Bessel functions of the first kind. The eigenvalues determine the Shannon channel capacity, regardless if the OAM modes or some other modes are chosen to realize spatial multiplexing. An estimate for the number of significant eigenvalues is given, which is asymptotically accurate for large radii (large relative to the transmission distance).

We then specialize the transmitting and receiving antenna arrangements to be UCAs with the same number of Hertzian dipole antennas on each side. This corresponds essentially to spatial sampling of the current distribution and electrical field on the continuous CAs. We derive analytical expressions for the eigenmodes and eigenvalues for the resultant (spatially) discrete MIMO channel. It turns out that the discrete eigenmodes are simply sampled versions of the continuous eigenmodes. The discrete eigenvalues, on the other hand, depend on the continuous eigenvalues through aliasing and are given by infinite sums of the latter. Nevertheless, since only a finite number of continuous eigenvalues are significant, the sums can be truncated without much loss of precision. Clearly, the resulting spatially discrete Shannon capacity cannot exceed the spatially continuous Shannon capacity.

Finally, we replace the ideal Hertzian dipoles with half-wave strip dipole antennas and numerically solve the resulting electromagnetic (EM) problem with a method of moments (MoM) technique. This takes into account mutual coupling and embedded radiation patterns of the array elements. It is numerically shown that the full-wave EM simulation gives the same result as the theoretical analysis for sparsely spaced UCAs with 1 and 2 m radius and 1 km hop distance, operating at 70 GHz. For this UCA setup (with fixed radii and different numbers of antenna elements), we also compare the channel capacity with a setup using uniform linear arrays (ULAs) with optimally designed inter-element spacing. Using a down-scaled extreme setting, we show that in the case of have-wavelength spacing, which corresponds to severe spatial over-sampling, the derived eigenvalues deviate from the simulated ones due to a strong element mutual coupling.

LOS MIMO using OAM has been the subject of numerous papers, see, e.g., [3]–[5] and the references therein. Recent practical realizations of OAM-based MIMO communication is reported in [6]–[8]. The expressions derived in this paper can be used to fact-check claims found in the literature and

This project has received funding from the European Union's Horizon 2020 research and innovation programme under the Marie Skłodowska Curie Grant Agreement No. 887732 (H2020-MSCA-IF VoiiComm).

to guide the practical implementation of such systems. We study a monochromatic problem in this paper, but it should be noted that modes are frequency-dependent [9], which is important for practical implementation.

The main contribution of the paper includes a first-principle tutorial derivation of the Shannon channel capacity for perfectly aligned UCAs with Hertzian dipole antennas. In particular, we derive

- Expressions for the spatially continuous eigenvalues in the form of Bessel functions of the first kind;
- Expressions for the spatially discrete eigenvalues as aliased continuous eigenvalues.

Moreover, we verify using full-wave EM simulation with realistic dipole antennas that the derived expressions are accurate if the antennas are not densely placed on the UCAs.

II. Channel with Continuous Circular Antennas

A. LOS channel formulation

We study the wireless channel between two perfectly aligned continuous CAs, $\mathcal{A}_t$ and $\mathcal{A}_r$, separated by D meters, under free-space propagation conditions. Their radii are denoted by R_t and R_r, respectively. As shown in Fig. 1, the origin of the coordinate system is at the center of $\mathcal{A}_t$. We assume that the antennas support continuous electrical currents, i.e., the elementary source is the Hertzian dipole. We also limit the discussion to time-harmonic current sources with the $\exp(j\omega t)$ convention and denote the current at the point $\mathbf{s} \in \mathcal{A}_t$ by $\boldsymbol{\mathcal{J}}(\mathbf{s})$. Under these conditions, the electric field radiated by $\mathcal{A}_t$ can be obtained directly by solving Maxwell's equations. The separation of the two antennas is assumed to be large enough (i.e., $D \gg \lambda$, where λ is the wavelength) to ensure $\mathcal{A}_r$ to be located in the far field of any elementary source. Note that we do not assume $\mathcal{A}_r$ to be in the far field of $\mathcal{A}_t$. Then at a generic position $\mathbf{p} \in \mathcal{A}_r$, the electric field can be expressed immediately via the Green's function method:

$$\boldsymbol{\mathcal{E}}(\mathbf{p}) = \int_{\mathcal{A}_t} \boldsymbol{\mathcal{G}}_{\mathrm{F}}(\mathbf{p}, \mathbf{s}) \boldsymbol{\mathcal{J}}(\mathbf{s}) \, \mathrm{d}\mathbf{s}. \tag{1}$$

In this expression, $\boldsymbol{\mathcal{G}}_{\mathrm{F}}(\mathbf{p}, \mathbf{s})$, the far-field dyadic Green's function, is given as follows [10, Appendix I] [11]:

$$\boldsymbol{\mathcal{G}}_{\mathrm{F}}(\mathbf{p}, \mathbf{s}) = \frac{-j\omega\mu}{4\pi r} e^{-j\frac{2\pi}{\lambda}r} \left(\mathbf{I} - \hat{\mathbf{r}}\hat{\mathbf{r}}^{\mathrm{T}}\right), \tag{2}$$

where $j = \sqrt{-1}$, μ the permeability of the free space, $r = \|\mathbf{r}\| = \|\mathbf{p} - \mathbf{s}\|$ is the distance from $\mathbf{s}$ to $\mathbf{p}$, $\hat{\mathbf{r}} = \mathbf{r}/r$ is the unit vector of the propagation direction, $(\cdot)^{\mathrm{T}}$ stands for transpose, and $\mathbf{I}$ is a 3×3 identity matrix. The measurement of the electric field using $\mathcal{A}_r$ is assumed to be ideal.

As illustrated in Fig. 1, $\mathbf{s}$ and $\mathbf{p}$ can be specified using two angles, $\theta_t, \theta_r \in [-\pi, \pi]$, respectively. In the selected coordinate system, their coordinate vectors are then given by $\mathbf{s}(\theta_t) = [R_t \cos\theta_t \; R_t \sin\theta_t \; 0]^{\mathrm{T}}$ and $\mathbf{p}(\theta_r) = [R_r \cos\theta_r \; R_r \sin\theta_r \; D]^{\mathrm{T}}$. Accordingly, r and $\hat{\mathbf{r}} = [\hat{r}_x \; \hat{r}_y \; \hat{r}_z]^{\mathrm{T}}$ are functions of (θ_t, θ_r):

$$r = \sqrt{D^2 + R_t^2 + R_r^2 - 2R_tR_r\cos(\theta_r - \theta_t)},$$
$$\hat{\mathbf{r}} = r^{-1}\left[R_r\cos\theta_r - R_t\cos\theta_t \quad R_r\sin\theta_r - R_t\sin\theta_t \quad D\right]^{\mathrm{T}}.$$

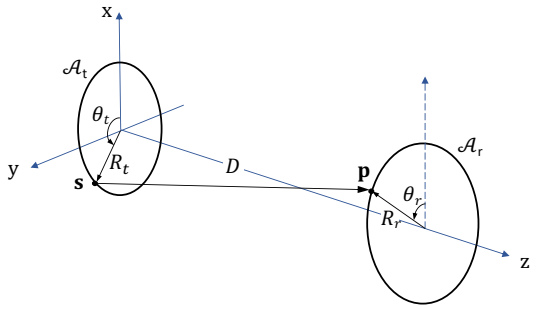

Fig. 1. LOS channel between two perfectly aligned circular arrays.

Although an arbitrarily polarized EM field can be generated following the assumptions above, for ease of discussion, we fix the orientation of the Hertzian dipoles in the x direction. In particular, the current at $\mathbf{s}(\theta_t)$ is assumed to be given by $\boldsymbol{\mathcal{J}}(\theta_t) = x(\theta_t)\hat{\mathbf{e}}_x$. Also, the electric field component in the x direction is measured[1], which can be considered as a one-dimensional spatial signal of θ_r, denoted by $y(\theta_r)$:

$$y(\theta_r) = \int_{-\pi}^{\pi} x(\theta_t) g_{x,x}(\theta_r, \theta_t) \mathrm{d}\theta_t \tag{3}$$

where

$$g_{x,x}(\theta_r, \theta_t) = \frac{-j\omega\mu R_t}{4\pi r}(1 - \hat{r}_x^2) e^{-j\frac{2\pi}{\lambda}r}, \tag{4}$$

and note that the dependence of r and $\hat{r}_x$ on (θ_t, θ_r) is omitted for clarity.

When $D \gg R_t$ and $D \gg R_r$,

$$\begin{aligned} r &\approx \sqrt{D^2 + R_t^2 + R_r^2} - \frac{R_tR_r}{\sqrt{D^2 + R_t^2 + R_r^2}}\cos(\theta_r - \theta_t) \\ &\approx D + \frac{\sqrt{R_t^2 + R_r^2}}{2D} - \frac{R_tR_r}{D}\cos(\theta_r - \theta_t), \end{aligned} \tag{5}$$

and $\hat{\mathbf{r}} \approx (0, 0, 1)$. Adopting (5) for the complex exponential term of $g_{x,x}(\theta_r, \theta_t)$ in (4), and $\hat{r}_x \approx 0$ and $r \approx D$ for the amplitude, the measured signal $y(\theta_r)$ can be approximated as

$$y(\theta_r) \approx G \int_{-\pi}^{\pi} x(\theta_t) h(\theta_r - \theta_t) \mathrm{d}\theta_t, \tag{6}$$

where

$$h(\theta) \triangleq e^{j\beta\cos\theta}, \tag{7}$$

with

$$\begin{cases} \beta \triangleq 2\pi\frac{R_tR_r}{\lambda D}, \\ G \triangleq \frac{-j\omega\mu R_t}{4\pi D}\exp\left(-j\frac{2\pi}{\lambda}\left(D + \frac{\sqrt{R_t^2+R_r^2}}{2D}\right)\right). \end{cases} \tag{8}$$

The linear mapping (6) is an analytical description of the LOS channel between the two continuous antennas under the large separation condition, and $G \cdot h(\theta_r)$ is its impulse response.

[1]The electric field components in the y and z directions are given by expressions same as (3), but having $(1 - \hat{r}_x^2)$ in $g_{x,x}(\theta_r, \theta_t)$ replaced by $(0 - \hat{r}_x\hat{r}_y)$ and $(0 - \hat{r}_x\hat{r}_z)$, respectively. Therefore, as D becomes large, $\hat{r}_y$ and $\hat{r}_z$ tend to 0, and y and z components become negligible.

B. Eigenmodes analysis

We reformulate (6) as

$$y_{\rm p}(\theta_r) = G\int_{-\infty}^{\infty} x_{\rm p}(\theta_t)\,\Pi\Big(\frac{\theta_t}{2\pi}\Big)\,h(\theta_r-\theta_t)\mathrm{d}\theta_t \tag{9}$$

where $\Pi(u)=1$ for $|u|\le 1/2$ and $\Pi(u)=0$ otherwise, and $h(\theta)$, $x_{\rm p}(\theta_t)$, and $y_{\rm p}(\theta_r)$ are periodic functions with period 2π. In particular, $x(\theta_t)$ and $y(\theta_r)$ are simply given by $x(\theta_t) = x_{\rm p}(\theta_t)\Pi\big(\frac{\theta_t}{2\pi}\big)$ and $y(\theta_r) = y_{\rm p}(\theta_r)\Pi\big(\frac{\theta_r}{2\pi}\big)$.

Due to the periodicity of $h(\theta)$, it can be represented by a Fourier series that is valid for all θ:

$$h(\theta) = \sum_{l=-\infty}^{\infty} C_l(\beta)e^{jl\theta}. \tag{10}$$

Since $h(\theta)$ can also be written as $h(\theta) = e^{j\beta\sin(\theta+\frac{\pi}{2})}$, we obtain

$$C_l(\beta) \triangleq \frac{1}{2\pi}\int_{-\pi}^{\pi} e^{j\beta\sin(\theta+\frac{\pi}{2})}e^{-jl\theta}\mathrm{d}\theta = j^l J_l(\beta) \tag{11}$$

where

$$J_l(\beta) \triangleq \frac{1}{2\pi}\int_{-\pi}^{\pi} e^{j(\beta\sin\theta - l\theta)}\mathrm{d}\theta \tag{12}$$

is the Bessel function of the first kind of the lth order. Similarly, $x_{\rm p}(\theta_t)$ can also be given by a Fourier series expansion $x_{\rm p}(\theta_t) = \sum_{m=-\infty}^{\infty} a_n e^{jm\theta_t}$.

It can be easily verified that

$$\big\{\psi_l(\theta) \triangleq e^{jl\theta}, l = 0, \pm1, \pm2, \dots\big\} \tag{13}$$

are the eigenfunctions of the linear mapping (9), and

$$\big\{\gamma_l(\beta) \triangleq 2\pi j^l G J_l(\beta), l = 0, \pm1, \pm2, \dots\big\} \tag{14}$$

are the corresponding eigenvalues. To prove this, one can substitute $x_{\rm p}(\theta_t) = e^{jl_0\theta_t}$ into (9), where l_0 can be any integer, and this will leads to

$$\begin{aligned} y_{\rm p}(\theta_r) &= G\int_{-\infty}^{\infty} e^{jl_0\theta_t}\Pi\Big(\frac{\theta_t}{2\pi}\Big)\left[\sum_{l=-\infty}^{\infty} C_l e^{jl(\theta_r-\theta_t)}\right]\mathrm{d}\theta_t \\ &= G\sum_{l=-\infty}^{\infty}\left[C_l e^{jl\theta_r}\int_{-\infty}^{\infty}\Pi\Big(\frac{\theta_t}{2\pi}\Big)e^{j(l_0-l)\theta_t}\mathrm{d}\theta_t\right] \\ &= G\sum_{l=-\infty}^{\infty}\left[C_l e^{jn\theta_r}\cdot 2\pi\,\mathrm{sinc}(l_0-l)\right] \\ &= 2\pi G\, C_{l_0} e^{jl_0\theta_r}, \end{aligned} \tag{15}$$

where the sinc function is defined as $\mathrm{sinc}(x) \triangleq \frac{\sin(\pi x)}{\pi x}$. This, by definition, proves that $\{\psi_l(\theta)\}$ and $\{\gamma_l(\beta)\}$ are the eigenfunctions and eigenvalues of the linear mapping (9).

Remark 1. *The above eigenfunction analysis shows that the OAM modes, i.e., the harmonic waves of θ, with the fundamental frequency given by $\frac{1}{2\pi}$, are the eigenmodes of the LOS channel between two continuous CAs. We refer [12] for a detailed definition of eigenmodes. Moreover, it is known that the far-field radiation of a UCA with a very large number of antennas can be approximately expressed as a superposition of OAM modes, and the weights are expressions of the Bessel functions of the first kind [4, Eq. (8)].*

C. Channel capacity and discussion

Given the total transmit power P, signal bandwidth B, and additive white Gaussian channel noise with power spectral density $N_0/2$, the Shannon channel capacity for the LOS channel (6) between two continuous CAs is

$$C_{\rm CA} = B\sum_{l=-\infty}^{\infty}\log\left(1+\frac{P_l^*|\gamma_l(\beta)|^2}{N_0 B}\right) \quad \text{[bit/s]} \tag{16}$$

where $\{P_l^*\}$ are obtained by waterfilling power allocation under the total power restriction [13, Chapter 7.1.1].

For a given β only a finite number of eigenvalues will be significant, as $J_l(\beta)\to 0$ as $|l|\to\infty$. That is, we can symmetrically truncate the sum in (16) to $K_0 = 2L_{\max}+1$ terms without essential loss of precision. We refer to K_0 as the effective number of degrees of freedom.

An estimate of K_0 can be obtained by viewing $h(\theta)$ as a phase-modulated signal with sinusoidal modulation (of frequency $f_m = \frac{1}{2\pi}$). Then β is the phase modulation index of $h(\theta)$, and Carson's rule gives us a rule-of-thumb estimation of its effective bandwidth [14, Eq. (5-61)]:

$$B_T = 2(\beta+1)f_m, \tag{17}$$

in which 98% of the total power is contained. Sampling $h(\theta)$ at the spacing of $1/B_T$ in its valid range $[-\pi,\pi]$ yields approximately $2\pi B_T = 2(\beta+1)$ samples. Since this value is not necessarily an integer, we suggest to adopt

$$\hat{K}_0 = 2\lceil\beta+1\rceil+1 \tag{18}$$

as an estimate of the effective number of DoF. Note that the estimation can be expected to be good for large β.

Finally, a known result: When β is a very small value, which happens when the separation of the two arrays are very large relative to the radii, $J_l(\beta)\approx 0$ for all non-zero l, and only the $l=0$ mode can be admitted ($J_0(\beta)\approx 1$).

III. Channel with Uniform Circular Arrays

Based on the analysis in the previous section, we extend the study to the spatially discrete MIMO channel between two UCAs with the same number of antennas on each side.

A. Discrete channel formulation

We discretize the problem by first assuming a finite number, N, x-oriented Hertzian dipoles with $x[n]$ current moment that are uniformly placed on the transmitting array, at $\theta_t = \frac{2\pi}{N}n$, $n = 0, 1, \dots, N-1$. As a result, $x(\theta_t)$ can be expressed as

$$x(\theta_t) = \sum_{n=0}^{N-1} x[n]\delta\Big(\theta_t - \frac{2\pi}{N}n\Big), \tag{19}$$

where $\delta(\cdot)$ is the Dirac delta function. Following (6), the generated electric field in the x direction on the continuous receiving CA is given by

$$y(\theta_r) = G\sum_{n=0}^{N-1} x[n]\int_{-\pi}^{\pi} h(\theta_r-\theta_t)\delta\Big(\theta_t-\frac{2\pi}{N}n\Big)\,\mathrm{d}\theta_t$$
$$= G\sum_{n=0}^{N-1} x[n]h\Big(\theta_r-\frac{2\pi}{N}n\Big). \tag{20}$$

Measuring $y(\theta_r)$ using N x-oriented Hertzian dipoles at $\theta_r = \frac{2\pi}{N}m$, $m = 0,1,\ldots,N-1$, we obtain

$$y[m] \triangleq y\Big(\frac{2\pi}{N}m\Big) = G\sum_{n=0}^{N-1} x[n]\,h[m-n], \tag{21}$$

where $h[m-n] \triangleq h\big(\frac{2\pi}{N}(m-n)\big)$. Equivalently, a pair of UCAs are formed, and this discrete linear equation (21) describes the LOS channel between them.

We remark that by forming two length-N column vectors $\mathbf{x} = [x[0]\cdots x[N-1]]^{\mathrm{T}}$ and $\mathbf{y} = [y[0]\cdots y[N-1]]^{\mathrm{T}}$, (21) can be expressed in the familiar matrix form:

$$\mathbf{y} = G\cdot\mathbf{H}\mathbf{x}. \tag{22}$$

where $\mathbf{H}$ has elements $[\mathbf{H}]_{m,n} = h[m-n]$ for $m,n = 0,1,\ldots,N-1$. It is easy to verify that $\mathbf{H}$ is a circulant matrix.

B. Eigenmode analysis

Adopting the Fourier series expansion (10) for $h(\theta)$, we obtain for $n = 0,1,\ldots,N-1$,

$$h[n] = h\Big(\frac{2\pi}{N}n\Big) = \sum_{l=-\infty}^{\infty} C_l(\beta)e^{jl\frac{2\pi}{N}n}. \tag{23}$$

Owing to the periodicity of $h(\theta)$, we have $h[n] = h[n \bmod N]$ for an arbitrary integer n. In addition, $e^{jl\frac{2\pi}{N}n} \equiv e^{j(l+kN)\frac{2\pi}{N}n}$ for any integer k. As a result, $h[n]$ can be further written as

$$h[n] = \frac{1}{N}\sum_{l=0}^{N-1} H_N[l]e^{j\frac{2\pi}{N}ln} \tag{24}$$

where

$$H_N[l] \triangleq N\sum_{k=-\infty}^{\infty} C_{l+kN}(\beta) = N\sum_{k=-\infty}^{\infty} j^{l+kN}J_{l+kN}(\beta). \tag{25}$$

Note that the dependence of $H_N[l]$ on β is omitted for brevity. From (24), we see that the sequences $\{h[n], n = 0,1,\ldots,N-1\}$ and $\{H_N[l], l = 0,1,\ldots,N-1\}$ form a Discrete Fourier Transform (DFT) pair.

We now proceed to show that the sampled version of the eigenmodes of the continuous channel are in fact the eigenmodes of the discrete channel. Substituting (24) and $x[n] = e^{j\frac{2\pi}{N}l_0n}$, $l_0 \in \{0,1,\ldots,N-1\}$, into (21) yields

$$y[m] = G\sum_{n=0}^{N-1} e^{j\frac{2\pi}{N}l_0n}\left(\frac{1}{N}\sum_{l=0}^{N-1} H_N[l]e^{j\frac{2\pi}{N}l(m-n)}\right)$$
$$= G\sum_{l=0}^{N-1} H_N[l]\left(\frac{1}{N}\sum_{n=0}^{N-1} e^{j\frac{2\pi}{N}[l(m-n)+l_0n]}\right)$$
$$= GH_N[l_0]e^{j\frac{2\pi}{N}l_0m}. \tag{26}$$

Hence, the discrete eigenfunctions (eigenvectors) and corresponding eigenvalues for the discrete linear mapping (21) are

$$\boldsymbol{\psi}_l \triangleq \begin{bmatrix} e^{j\frac{2\pi}{N}l\cdot 0} & e^{j\frac{2\pi}{N}l\cdot 1} & \ldots & e^{j\frac{2\pi}{N}l\cdot(N-1)}\end{bmatrix}^{\mathrm{T}} \tag{27}$$

$$\gamma_l^{\mathrm{s}}(\beta) = G\cdot H_N[l] = NG\sum_{k=-\infty}^{\infty} j^{l+kN}J_{l+kN}(\beta), \tag{28}$$

for $l = 0,1,\ldots,N-1$. Note that $\{|\gamma_l^{\mathrm{s}}(\beta)|\}$ are the unsorted singular values of this channel.

Remark 2. *Forming the N eigenvectors into a matrix:*

$$\boldsymbol{\Psi}_N = \begin{bmatrix}\boldsymbol{\psi}_0 & \boldsymbol{\psi}_1 & \ldots & \boldsymbol{\psi}_{N-1}\end{bmatrix}, \tag{29}$$

following (26), we can immediately obtain that

$$\mathbf{H}\boldsymbol{\Psi}_N = \boldsymbol{\Psi}_N\cdot\mathrm{diag}\big(H_N[0],H_N[1],\ldots,H_N[N-1]\big) \tag{30}$$

where the operator $\mathrm{diag}(\cdot)$ *forms the sequence in the bracket into a diagonal matrix. Note that $\boldsymbol{\Psi}_N$ (or $\frac{1}{\sqrt{N}}\boldsymbol{\Psi}_N$) is exactly the $N\times N$ DFT matrix. The relation (30) suggests the adoption of $\boldsymbol{\Psi}_N$ as the precoding matrix and $\frac{1}{N}\boldsymbol{\Psi}_N^{\mathrm{H}}$ as the combining matrix, for the interference-free transmission of N parallel data streams over this particular discrete LOS MIMO channel.*

A singular value decomposition (SVD) of $\mathbf{H}$ can be directly obtained based on (30) [5]. Based on the fact that a circulant matrix can be diagonalized by the DFT matrix, the eigenvalues of $\mathbf{H}$ have been derived in [5] but in a less interpretable expression. In addition, it has been shown in [1] that for $N\to\infty$, the singular values (magnitudes of the eigenvalues in this case) of $\mathbf{H}$ are proportional to $|J_l(\beta)|$ [1, Theorem 1]. Our analysis reveals the relation between eigenvalues and Bessel functions for the general situation, i.e., for any N.

C. Channel capacity and discussion

Under the same transmit power, bandwidth, and channel noise assumptions as in the continuous case, the Shannon channel capacity for this discrete MIMO channel (21) is

$$C_{\mathrm{UCA}} = B\sum_{l=0}^{N-1}\log\left(1+\frac{P_l^*|\gamma_l^{\mathrm{s}}(\beta)|^2}{N_0B}\right)\quad[\text{bit/s}], \tag{31}$$

where $\{P_l^*\}$ are again found by waterfilling power allocation.

As Section III-A shows, the formulation of the discrete channel between two UCAs corresponds to spatial sampling of the current distribution on the transmitting circular array and the electric field on the receiving array. Moreover, as discussed in Section II-C, the effective bandwidth of the spatial channel is essentially limited. As a result, given an odd integer N that

satisfies $N \geq K_0$, where K_0 is the effective number of DoF of the continuous channel, we will have the following:

$$\gamma_l^{\mathrm{s}}(\beta) \approx \begin{cases} NG\, j^l J_l(\beta), & l = 0, 1, \ldots, \frac{N-1}{2} \\ NG\, j^{l-N} J_{l-N}(\beta), & l = \frac{N+1}{2}, \ldots, N-1. \end{cases} \tag{32}$$

Otherwise, an under-sampling situation is faced, and the discrete eigenvalues become proportional to infinite sums of the continuous eigenvalues due to aliasing.

We also note that no extra spatial DoF can be achieved by adding more antennas than needed, and the total number of spatial DoF available in the channel is determined by the geometry—radii and the distance of the arrays—though the β parameter. Although more Hertzian dipoles will always increase the eigenvalues' magnitude (see the N multiplier in (28)), deterioration will be caused by practical effects, mutual coupling in particular, when the spacing between the actual physical antennas becomes dense.

IV. Numerical Study

For numerical evaluation, we consider two identical and perfectly aligned UCAs, separated by 1 kilometer apart ($D = 1$ km), operating at 70 GHz. We consider two options for the radius: $R = 1$ or 2 meters ($R_t = R_r = R$), which corresponds to $\beta = \beta_1 \approx 1.466$ and $\beta = \beta_2 \approx 5.864$ following (8). This setting may represent the geometry of a wireless transport link.

Fig. 2 presents the curves of $J_n(\beta)$ for nonnegative integer orders up to 13. From their intersections with the two vertical lines: $\beta = \beta_1$ and $\beta = \beta_2$, one can immediately obtain the number of significant eigenvalues of the continuous channel and their relative magnitudes. Following the discussions in Section II-C, we expect the values of $|J_n(\beta)|$ to be small for those $n > \lceil \beta + 1 \rceil$ ($\lceil \beta_1 + 1 \rceil = 3$, $\lceil \beta_2 + 1 \rceil = 7$). The intersections show that they are reasonable estimates.

In Fig. 3, we compare $\frac{1}{N}|H_N[l]|$, which indicates the relative size of the singular values, for the two radii and $N = 4, 5, \ldots, 10$. The results, presented in dB in decreasing order[2], are obtained via two approaches. In the first approach, $\{H_N[l]\}$ are obtained by performing DFT is performed to $\{h[n]\}$, where $h[n] = \exp(-j\beta\cos(\frac{2\pi}{N}n))$; in the second approach, the results are obtained by

$$\frac{1}{N}\left|H_N[l]\right| = \left|\sum\nolimits_{k=-K_{\max}}^{K_{\max}} j^{-(l+kN)} J_{l+kN}(\beta)\right|, \tag{33}$$

where $K_{\max}$ is set to be the smallest integer satisfying $K_{\max}N \geq 1000$ for any N. Good agreement between the two approaches can be seen. Following (18), the estimated effective number of DoF is $\hat{K}_0 = 7$ and 15 for the two radii. As a result, in Fig. 3 (a), a large part of the curves collide for large N, while in Fig. 3 (b), the curves deviate from each other due to the N and l dependent, constructive or destructive, superposition following (33). We can also see that when using 4 and 7 antennas for the two radii, relatively uniformly distributed singular values are resultant.

[2]In Fig. 3 and Fig. 4, results are presented in decreasing magnitude order. We emphasize that the indices shown on the x-axis of all inclusion plots do NOT correspond to the indices of the discrete eigenmodes.

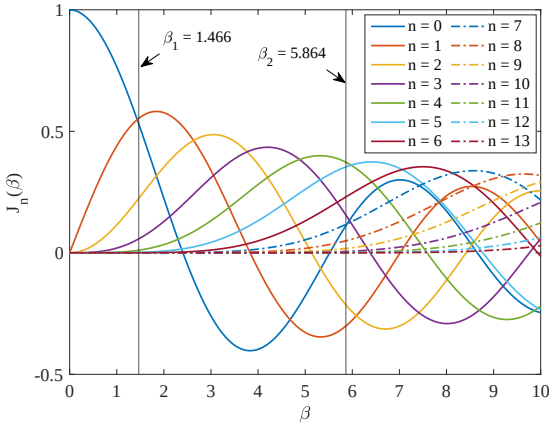

Fig. 2. The value of $J_n(\beta)$ for different non-negative orders. For negative orders, $J_{-n}(\beta) = (-1)^n J_n(\beta)$.

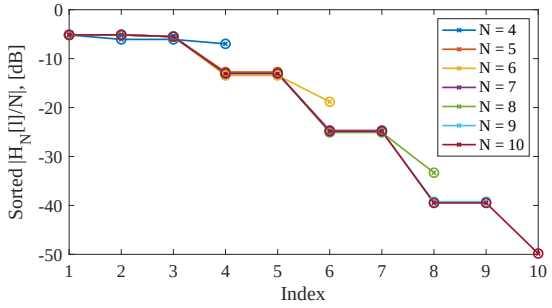

(a) $R = 1$ m

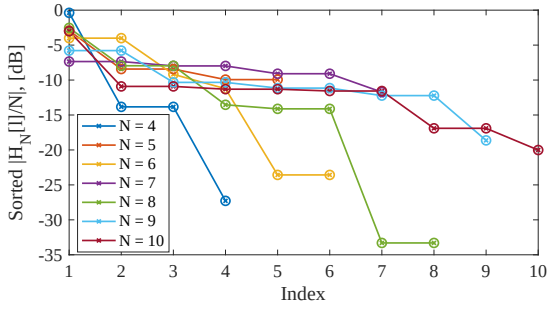

(b) $R = 2$ m

Fig. 3. Comparison of $\frac{1}{N}|H_N[l]|$ [dB] in decreasing order for different N. The 'cross' markers represents the results given by DFT; the 'circle' markers represents the results obtained by (33).

We examine the derived eigenvalue expressions by performing full-wave EM simulations with half-wave strip dipole antennas (orientated in the x-direction) under the same geometric setting with $N = 10$ and a down-scaled setting that represents an extreme situation: R is fixed to be 0.02 m, D is set to be 0.4 m and 0.1 m such that β_1 and β_2 are again resultant, and $N = 58$ is chosen such that the antenna spacing is approximately $\lambda/2$ (at 70 GHz). The in-house developed MoM code, employing the Galerkin method to solve the corresponding mixed potential integral equation with Rao-Wilton-Glisson (RWG) basis [15], was used at this stage. This simulation takes into account antenna mutual coupling and embedded element pattern of the dipole arrays, and produces

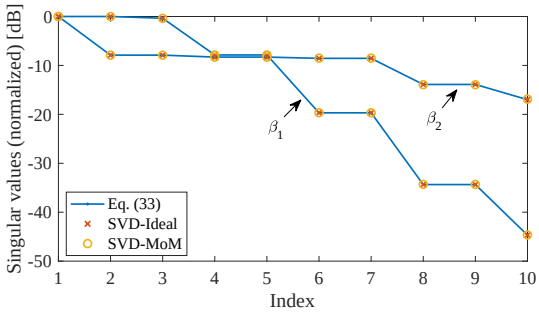

(a) $R = 1$ or 2 m, $D = 1$ km, $N = 10$

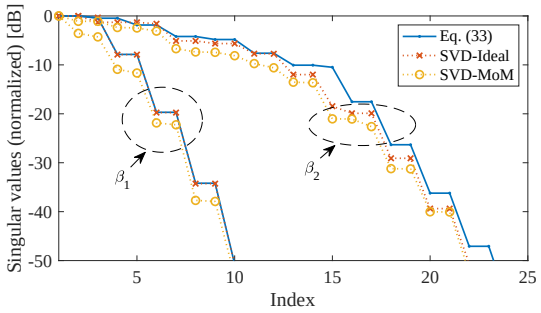

(b) $R = 0.02$ m, $D = 0.4$ or 0.1 m, $N = 58$

Fig. 4. Singular values [dB] obtained by different approaches. The results are normalized using the largest singular value in each setting/approach.

the full antenna system S-matrix, from which singular values are found by SVD of the channel matrix (a block of the S-matrix). We also compute the singular values of the ideal channel matrix formed according to (4), i.e., using the exact r and $\hat{r}_x$ to obtain the entries. These simulated singular values, as well as $\frac{1}{N}|H_N[l]|$ given by (33), are compared in Fig. 4.

As the results show, for the default setting with very sparse antenna placement, the singular values obtained via different approaches agree very well. For the down-scaled setting, however, the mutual coupling effects cause a few dB loss in the singular values obtained by the EM simulation, as compared with those of the ideal channel. Physically the effects can be attributed to the increased reflected power in the transmitting array that occurs when generating higher-order OAM modes (similar to the scan loss phenomenon in conventional array antennas). Furthermore, when $D = 0.1$ m, gaps between the calculated singular values of the ideal channel and those given by (33) can also be seen. This is because the approximations for r and $\hat{\mathbf{r}}$ adopted for the channel formulation (6) and (7) causes non-negligible errors, since R and D become comparable in this case.

Finally, the channel capacity performances for the default UCA settings (with fixed radii and a varying N), are compared with those for a setting where a pair of identical ULAs are adopted (with the same the hop distance). The spacing of the ULA, denoted by δ_{ULA}, is optimally designed following [16]:

$$\frac{\delta_{\text{ULA}}^2}{\lambda D} = \frac{1}{N}, \tag{34}$$

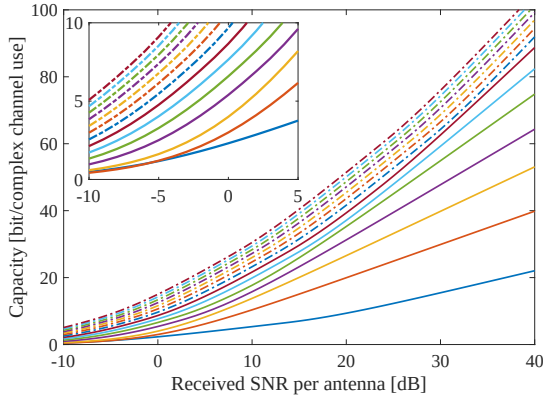

(a) UCA, $R = 1$ m

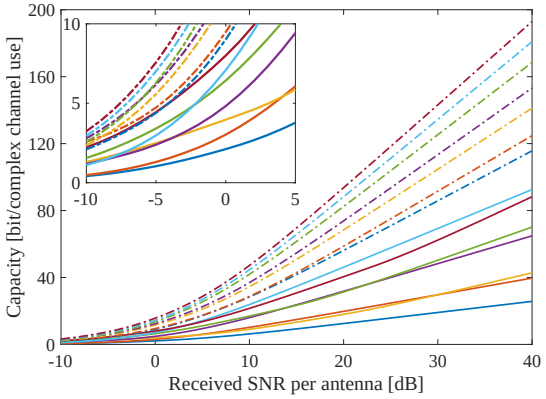

(b) UCA, $R = 2$ m

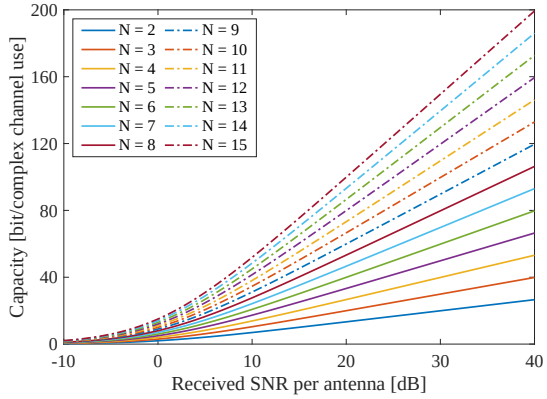

(c) Optimally designed ULA

Fig. 5. Comparison of the channel capacity.

resulting an increasing array length with N, given by

$$L_{\text{ULA}}(N) = \frac{N-1}{\sqrt{N}}\sqrt{\lambda D}. \tag{35}$$

With the optimal design, N identical singular values of the LOS channel (since $D \gg L_{\text{ULA}}$) can be expected.

The channel capacity curves are plotted against the received SNR per antenna in Fig. 5, and the curve legend can be found in subfigure (c). From Fig. 5 (a) and Fig. 5 (b), it can be seen that, in general, for a given received SNR, the channel capacity for the fixed-radius UCA case does not necessarily

TABLE I
CHANNEL CAPACITY [BIT/COMPLEX CHANNEL USE] FOR DIFFERENT SETUPS AT 35 DB RECEIVED SNR PER ANTENNA.

N		4	7	11	15
C_{UCA}	$R = 1$, $C_\circ = 6.28$ [m]	46.4	70.8	82.4	90.2
	$R = 2$, $C_\circ = 12.57$ [m]	36.2	80.9	122.9	168.0
C_{ULA}		46.5	81.4	127.9	174.4
L_{ULA} [m]		3.11	4.69	6.24	7.48

grow with N. Fundamentally guided by the singular value distributions following (28), when $R = 1$ m, essentially no more DoF is achieved when $N \geq 8$, but only a small power gain by each increased antenna; while for $R = 2$ m, many crossings between the capacity curves can be observed in Fig. 5 (b). On the other hand, owing to the optimally designed antenna spacing and the increasing aperture, each additional pair of antennas in the ULAs brings an extra spatial DoF and multiplexing gain to the MIMO channel.

When serving as a wireless backhaul link with 1 GHz bandwidth, the high SNR range (e.g., 30 to 40 dB) is of practical interest, considering the actual path loss, typical gains for small commercial E-band (70/80 GHz) antennas, noise figure, margin for fading, etc. In Table I, the channel capacity results achieved at 35 dB received SNR per antenna under several selected settings are presented. For the UCA setup with $R = 1$ m and $N = 4$, or with $R = 2$ m and $N = 7$, good singular value distributions are achieved, as shown by Fig. 3. As expected, the channel capacity results are close to those with ULAs with the same number of antennas. When $N = 11$, the length, L_{ULA}, of the optimally designed ULA is approximately equal to the circumference, $C_\circ$, of the UCA with radius 1 m, but the capacity it brings is much higher than that of the latter (by about 40 [bit/complex channel use]). In fact, the capacity of the ULA ($N = 11$) is also larger than the capacity of the bigger UCA with 2 m radius (by about 5 [bit/complex channel use]). For UCAs with 2 m radius ($C_\circ = 12.57$ m) and $N = 15$, which is the estimated effective number of DoF in this case, the capacity performance is slightly below the smaller ULA ($L_{\text{ULA}} = 7.48$ m) thanks to the closely approaching spatial multiplexing gain for high SNR range.

V. CONCLUSION

For perfectly aligned CAs with transmit radius R_t, receive radius R_r, transmission distance D, and monochromatic transmission at wavelength λ, the channel eigenmodes and eigenvalues are shown to be given by (13) and (14) when $D \gg \max\{R_t, R_r\}$. The lth eigenvalue is $AJ_l(\beta)$, where A is constant, $J_l(\cdot)$ is the Bessel function of the first kind and order l, and $\beta = 2\pi R_t R_d/(\lambda D)$. The effective number of eigenmodes (i.e., the number of modes with non-negligble eigenvalues) can estimated as $\hat{K}_0 = 2\lceil \beta + 1 \rceil + 1$.

By interpreting UCAs as spatially sampled CAs, we derived formulas for computing the UCA channel eigenmodes and eigenvalues from the CA channel counterparts, see (27) and (28). This allows us to specify analytical expressions for the eigenvalues for the $N \times N$ UCA LOS MIMO channel, which offers considerably more insight than the method of numerically computing the channel matrix SVD. Moreover, $\hat{K}_0$ gives an estimate of the channel matrix rank and thereby the smallest number of antennas required for harvesting (essentially) all available spatial streams. The analytical results agree with full-wave electromagnetic simulations (which take into account antenna mutual coupling and embedded element pattern) for the considered geometries: $R_t = R_r = 1, 2$ m, $D = 1$ km, carrier frequency 70 GHz, which are reasonable for wireless transport links. Finally, it can be shown that, for medium to large SNR and same number of antennas, a ULA with optimum antenna spacing (34) has significantly higher channel capacity compared to the UCA whose circumference is equal to the ULA length.

REFERENCES

[1] P. Wang, Y. Li, and B. Vucetic, "Millimeter wave communications with symmetric uniform circular antenna arrays," *IEEE communications letters*, vol. 18, no. 8, pp. 1307–1310, 2014.

[2] Y. Jeon, G.-T. Gil, and Y. H. Lee, "Design and analysis of LoS-MIMO systems with uniform circular arrays," *IEEE Transactions on Wireless Communications*, vol. 20, no. 7, pp. 4527–4540, 2021.

[3] B. Thidé, H. Then, J. Sjöholm, K. Palmer, J. Bergman, T. Carozzi, Y. N. Istomin, N. Ibragimov, and R. Khamitova, "Utilization of photon orbital angular momentum in the low-frequency radio domain," *Physical Review Letters*, vol. 99, no. 8, p. 087701, 2007.

[4] S. M. Mohammadi, L. K. Daldorff, J. E. Bergman, R. L. Karlsson, B. Thidé, K. Forozesh, T. D. Carozzi, and B. Isham, "Orbital angular momentum in radio—a system study," *IEEE Transactions on Antennas and Propagation*, vol. 58, no. 2, pp. 565–572, 2009.

[5] O. Edfors and A. J. Johansson, "Is orbital angular momentum (OAM) based radio communication an unexploited area?" *IEEE Transactions on Antennas and Propagation*, vol. 60, no. 2, pp. 1126–1131, 2011.

[6] D. Lee, H. Sasaki, H. Fukumoto, Y. Yagi, and T. Shimizu, "An evaluation of orbital angular momentum multiplexing technology," *Applied Sciences*, vol. 9, no. 9, p. 1729, 2019.

[7] Y. Yagi, H. Sasaki, T. Yamada, and D. Lee, "200 Gb/s wireless transmission using dual-polarized OAM-MIMO multiplexing with uniform circular array on 28 GHz band," *IEEE Antennas and Wireless Propagation Letters*, vol. 20, no. 5, pp. 833–837, 2021.

[8] M. Hirabe, R. Zenkyu, H. Miyamoto, K. Ikuta, and E. Sasaki, "40 m transmission of OAM mode and polarization multiplexing in E-band," in *2019 IEEE Globecom Workshops (GC Wkshps)*, 2019, pp. 1–6.

[9] T. Ingason, H. Liu, M. Coldrey, A. Wolfgang, and J. Hansryd, "Impact of frequency selective channels on a line-of-sight MIMO microwave radio link," in *IEEE 71st Vehicular Technology Conference*, 2010, pp. 1–5.

[10] A. S. Poon, R. W. Brodersen, and D. N. Tse, "Degrees of freedom in multiple-antenna channels: A signal space approach," *IEEE Transactions on Information Theory*, vol. 51, no. 2, pp. 523–536, 2005.

[11] L. Ding, E. G. Ström, and J. Zhang, "Degrees of freedom in 3D linear large-scale antenna array communications—a spatial bandwidth approach," *IEEE Journal on Selected Areas in Communications*, early access, doi: 10.1109/JSAC.2022.3196106.

[12] D. A. Miller, "Waves, modes, communications, and optics: a tutorial," *Advances in Optics and Photonics*, vol. 11, no. 3, pp. 679–825, 2019.

[13] D. Tse and P. Viswanath, *Fundamentals of wireless communication*. Cambridge university press, 2005.

[14] L. W. Couch, *Digital and analog communication systems*. Prentice-Hall, 1997.

[15] S. Rao, D. Wilton, and A. Glisson, "Electromagnetic scattering by surfaces of arbitrary shape," *IEEE Transactions on Antennas and Propagation*, vol. 30, no. 3, pp. 409–418, 1982.

[16] F. Bøhagen, P. Orten, and G. E. Øien, "Design of optimal high-rank line-of-sight MIMO channels," *IEEE Transactions on Wireless Communications*, vol. 6, no. 4, pp. 1420–1425, 2007.